Single-atom tailoring of platinum nanocatalysts for high-performance multifunctional electrocatalysis

Mufan Li[1,2,13], Kaining Duanmu[3,13], Chengzhang Wan[1,13], Tao Cheng[4,5,13], Liang Zhang[6], Sheng Dai[7], Wenxin Chen[8], Zipeng Zhao[2], Peng Li[1], Huilong Fei[1], Yuanming Zhu[9], Rong Yu[9], Jun Luo[10], Ketao Zang[10], Zhaoyang Lin[1], Mengning Ding[2], Jin Huang[2], Hongtao Sun[1], Jinghua Guo[6], Xiaoqing Pan[7,11], William A. Goddard III[4], Philippe Sautet[1,3,12], Yu Huang[2,12*], Xiangfeng Duan[1,12*]*

[1]Department of Chemistry and Biochemistry, University of California, Los Angeles, Los Angeles, California 90095, USA; [2]Department of Materials Science and Engineering, University of California, Los Angeles, CA 90095, USA; [3]Department of Chemical and Biomolecular Engineering, University of California, Los Angeles, CA 90095, USA; [4]Materials and Process Simulation Center, California Institute of Technology, Pasadena, CA 91125, USA; [5]Institute of Functional Nano & Soft Materials (FUNSOM), Jiangsu Key Laboratory for Carbon-Based Functional Materials & Devices, Joint International Research Laboratory of Carbon-Based Functional Materials and Devices, Soochow University, Suzhou, Jiangsu, 215123, P. R. China; [6]Advanced Light Source, Lawrence Berkeley National Laboratory, Berkeley, CA 94720, *USA*; [7]Department of Materials Science and Engineering, University of California Irvine, Irvine, California 92697, USA; [8]Departmentof Chemistry, Tsinghua University, Beijing 100084, P. R. China; [9]National Center for Electron Microscopy in Beijing, School of Materials Science and Engineering, Tsinghua University, Beijing 100084, P. R. China; [10]Center for Electron Microscopy in Tianjin University of Technology, Tianjin 300384, P. R. China; [11]Irvine Materials Research Institute (IMRI), University of California Irvine, Irvine, California 92697, USA; [12]California NanoSystems Institute, University of California, Los Angeles, Los Angeles, California 90095, USA. [13]These authors contributed equally to this work.

[*]Correspondence to: xduan@chem.ucla.edu, yhuang@seas.ucla.edu, sautet@ucla.edu

Platinum-based nanocatalysts play a crucial role in various electrocatalytic systems that are important for renewable clean energy conversion, storage and utilizations. However, the scarcity and high cost of Pt seriously limit their practical application. Decorating Pt catalysts with other transition metals offers an effective pathway to tailor their catalytic property for specific reactions, but often at the sacrifice of the electrochemical active surface area (ECSA). Here we report a single-atom tailoring strategy to boost the activity of Pt nanocatalysts with minimal loss in surface active sites. By starting with PtNi alloy nanowires and using a partial electrochemical dealloying approach, we create single nickel atom modified Pt nanowires with an optimum combination of specific activity and ECSA for the hydrogen evolution,

methanol oxidation and ethanol oxidation reactions. The single-atom tailoring approach offers an effective strategy to optimize the activity of surface Pt atoms and enhance the Pt mass activity for diverse reactions and opens a general pathway to the design of highly-efficient and durable precious metal-based catalysts.

Platinum represents the most iconic element for various energy related electrocatalytic systems, such as hydrogen evolution reaction (HER), oxygen reduction reaction (ORR), methanol oxidation reaction (MOR) and ethanol oxidation reactions (EOR)[1-14]. The intrinsic electrocatalytic activity and stability of Pt make it the most widely studied material for diverse electrochemical reactions. However, its high cost and scarcity seriously limit the practical applications of the Pt-based electrocatalysts and widespread adoption of the relevant technologies. Thus, a central challenge for all the Pt-powered reactions is how to substantially reduce the required amount of Pt in the catalysts, which demands a major leap in Pt mass activity (MA) (*i.e.*, the catalytic current per unit mass of Pt).

The MA is fundamentally determined by the product of the electrochemically active surface area (ECSA, normalized by mass) and the specific activity (SA, catalytic current normalized by ECSA). Considerable efforts have been placed on improving the ECSA by tailoring various geometrical factors, including creating ultrafine nanostructures or core/shell nanostructures with an ultrathin Pt skin to expose most Pt atoms on the surface for catalytic reactions[15-21]. In parallel, intensive efforts have been devoted to optimizing the SA for various electrochemical processes by tuning the chemical compositions, exposed catalytic surface and surface topology[10,22-24]. In particular, surface modification/decoration of the existing Pt catalysts represents an interesting pathway to tailor the electrocatalytic activity. For example, combining Pt-based material with transition metal hydroxides (e.g., $Ni(OH)_2$) has been shown to greatly enhance SA for HER and MOR in alkaline electrolytes[13,25,26]. However, such modification inevitably blocks some surface active sites and often results in a relatively small ECSA (~20-60 m^2/g_{Pt}, typically with 30-50% lower than those without modification)[1,27]. This represents an intrinsic dilemma for the surface modification strategy, which may tailor the local electronic structure to boost the SA for a given reaction, but usually at a substantial sacrifice of the ECSA. Together, these competing factors make it extremely challenging to simultaneously achieve a high SA and a high ECSA in the same catalyst system, which is necessary for delivering a high MA.

In general, for Pt nanocatalysts decorated with a given transition metal (*e.g.*, nickel) species, in which the nickel-based nanostructures function as the catalyst promoter to enhance the catalytic activity of nearby surface Pt atoms, it is important to minimize the size of the decorating species to prevent unnecessary blockage of surface Pt sites while

creating the most activated Pt site with nickel neighbors for enhanced SA. In this regard, the ultimate limit of the decorating species are single atoms, which uses the smallest number of nickel species to activate the most Pt atoms while blocking the least amount of surface Pt sites to ensure the highest mass activity (Supplementary Fig. 1). However, the creation of single atom decorated Pt surface is challenging with typical synthetic approaches and has not been realized to date.

Herein, by starting with PtNi alloy nanowires and using a partial electrochemical dealloying approach, we create single atom nickel modified Pt nanowires (SANi-PtNWs) with abundant activated Pt sites next to SANi and minimal blockage of the surface Pt sites (Fig. 1), thus enabling a unique design of single atom tailored Pt electrocatalysts with an optimum combination of SA and ECSA to deliver high MA for diverse electrochemical reactions including hydrogen evolution reaction (HER), methanol oxidation reaction (MOR), and ethanol oxidation reaction (EOR), with high catalyst durability. Importantly, we show that the resulting SANi-PtNWs display a substantially increased MA of 11.8 ± 0.43 A/mg$_{Pt}$ for HER at -70 mV *vs.* RHE at pH 14 (comparing with the previous record of 3.03 A/mg$_{Pt}$)[3]. Density functional theory (DFT) calculations reveal that all Pt atoms around SANi show a reduced hydrogen binding energy and are optimal for HER. We further show that such single atomic modification also greatly enhances the catalytic activity for both MOR and EOR to deliver a mass activity of 7.93 ± 0.45 A/mg$_{Pt}$ and 5.60 ± 0.27 A/mg$_{Pt}$ (*vs.* previous records of 2.92 A/mg$_{Pt}$ and 2.95 A/mg$_{Pt}$)[6,9], respectively. These studies demonstrate that the single atom tailoring approach offers a general strategy for creating highly efficient electrocatalysts for diverse reactions.

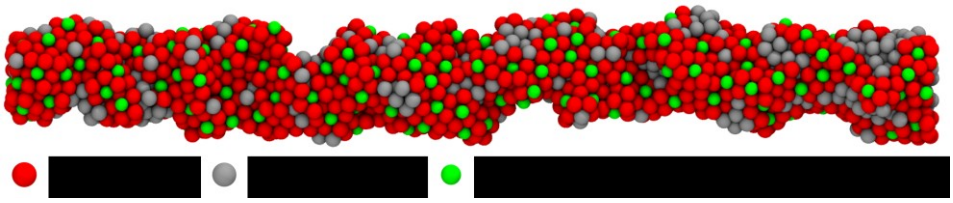

Fig. 1 | Schematic diagram for SANi-PtNWs. The decoration of ultrafine PtNWs with single atomic nickel species tailors the local electronic structure to boost the specific catalytic activity for diverse electrochemical reactions with minimal sacrifice in the number of surface active sites. Grey atoms represent regular Pt (111) surface sites, green atoms represent isolated Ni sites (Ni is liganded to two OH groups in electrocatalytic conditions), and red atoms represent activated Pt atoms with Ni neighbor as catalytically hot sites.

Results

Catalyst synthesis and characterizations. A simple one-pot synthetic procedure followed by an annealing process in argon/hydrogen mixture (Ar/H_2: 97/3) was used to produce the Ni rich PtNi alloy NWs (composition ~$Pt_{17}Ni_{83}$) with an average length of ~300 nm and diameter of ~4.5 nm (Supplementary Fig. 2a). The resulted PtNi NWs were

dispersed on carbon support in ethanol to form the catalyst ink, which was then cast onto glassy carbon rotating disk electrode (RDE, geometry area = 0.196 cm^2) to form a homogeneous film. An electrochemical dealloying process was performed via cyclic voltammetry (CV) between 0.05 V - 1.10 V *vs.* RHE in 0.1 M $HClO_4$ to gradually remove nickel species. The ECSA gradually increases with increasing number of CV cycles and eventually saturates at about 112.9 ± 5.4 m^2/g_{Pt} after 200 CV cycles (Supplementary Fig. 2c, d), which indicates the completion of dealloying process to obtain pure Pt NWs (pure-PtNWs)[10]. Such an ECSA evolution trend was also confirmed by acidic CO stripping experiments (Supplementary Fig. 2e, f). The average diameter is reduced from ~4.5 nm before to ~2.0 nm after the complete dealloying process (Supplementary Fig. 2b).

To tailor the nickel decoration in the resulting PtNWs, we interrupt the acidic CV dealloying process periodically to produce PtNWs with different amount of nickel decorating species, which was then transferred into nitrogen-saturated 1 M KOH for 100 additional CV cycles between 0.05 V – 1.6 V for further activation. The resulting dealloyed NWs with selectively decorated Ni species are generally stable in the basic conditions, in which their catalytic performance is evaluated. We have initially used HER as a model reaction to evaluate the activity of the resulting PtNW catalysts with varying amount of nickel species (Supplementary Fig. 2g) and discovered that a peak performance is achieved at 180 acidic dealloying CV cycles. Too much (<180 cycles) or too little (>180 cycles) nickel species would reduce the overall HER activity (Supplementary Fig. 2h). The produced Ni species are stable in basic conditions. We have thus focused our discussion on this optimum material produced with 180 dealloying CV cycles unless otherwise specifically mentioned.

High-angle annular dark-field scanning transmission electron microscope (HAADF-STEM) was conducted to probe the atomic structure of the resulting material. The HAADF-STEM shows an ultrafine 1D crystalline configuration with rich surface defects, concave cavity sites and steps as highlighted by white arrows (Fig. 2a). HAADF-STEM image shows that the (111) spacing is 0.225 nm (Fig. 2a), about 2.2 % smaller than that of crystalline Pt (0.230 nm). The composition analysis by inductively coupled plasma atomic emission spectrometry (ICP-AES) reveal an overall Pt:Ni ratio of 92:8 for SANi-PtNWs, corresponding to 2.4 Ni atoms per square nanometer surface area. Considering the Pt surface atom density around 15 Pt/nm^2, the surface Ni:Pt atom ratio is around 1:6. Electron energy loss spectroscopy (EELS) elemental mapping of Ni (Fig. 2b) and that overlaid on Pt HAADF contrast image (Fig. 2c) reveals that the nickel atoms are sparsely distributed on the PtNWs.

We have further conducted X-ray absorption fine structure (XAFS) and X-ray absorption near edge structure (XANES) measurements to probe the local atomistic and electronic structures. The oxidation state of Pt can be probed by the white line intensity at

Pt L_3-edge in XANES spectra[28,29]. The Pt XANES result shows that the white line intensity of our sample (Supplementary Fig. 3a) is close to that of a Pt foil, indicating that the average oxidation state of Pt is mostly zero. The Pt extended X-ray absorption fine structure (EXAFS) fitting result shows a main peak at about 2.74 Å (Fig. 2d, Supplementary Table 1), which is about 1.8 % smaller than the Pt-Pt bond length in bulk Pt (2.79 Å in Pt foil), consistent with the TEM studies described above and previous report[10].

The XANES for Ni K-edge provides information on the oxidation state of Ni species based on the absorption threshold position and white line intensity (due to the allowed 1s→4p transition)[30]. The Ni K-edge XANES in our optimum material closely resembles that of $Ni(OH)_2$ with slightly lower intensity (Supplementary Fig. 3b), suggesting the nickel species have an average oxidation state close to two, and primarily exists as surface decorating species (an oxidation state of zero is expected for the buried nickel). Further XPS studies also confirmed the 2+ oxidation state of the Ni species (Supplementary Fig. 3c). The Ni EXAFS shows a single peak at 1.6 Å (Fig. 2e, Supplementary Table 2), which can be attributed to the first shell Ni-O bond. There is no obvious peak at 2.1 Å (for Ni-Ni coordination in metallic Ni) or 2.7 Å (For Ni-O-Ni coordination in $Ni(OH)_2$) (Fig. 2e), strongly confirming that the Ni species exist as single atomic species without long range coordination to another Ni center. The XANES and EXAFS hence demonstrate the successful creation of single atom nickel modified PtNWs (SANi-PtNWs) catalysts. The EXAFS fitting details are described in Supplementary Figs. 4-5 and Supplementary Tables 1-2.

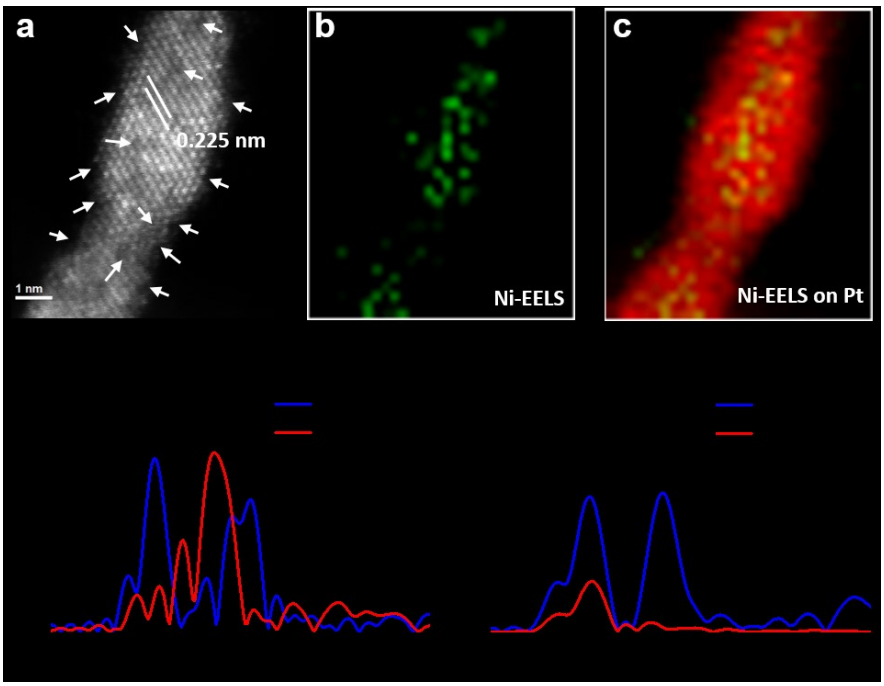

Fig. 2 | Structural characterization of the SANi-PtNWs. (**a**) HAADF-STEM image of

SANi-PtNWs, with the white arrows highlight the surface defects, steps and concave cavity sites. (**b**) Ni EELS mapping. (**c**) Overlaid image of Ni-EELS mapping on Pt, with red representing Pt and green representing Ni. (**d**) Pt EXAFS fitting result and (**e**) Ni EXAFS fitting result.

HER measurements of the SANi-PtNWs. The HER activity of the SANi-PtNWs was investigated by using the rotation disk electrode (RDE) test and compared against the fully dealloyed pure-PtNWs and the commercial Pt/C (10 wt%). The CV studies of the SANi-PtNWs show two exclusive Ni^{2+}/Ni^{3+} redox peaks at 1.321 V ($Ni^{3+} \rightarrow Ni^{2+}$) and 1.388 V ($Ni^{2+} \rightarrow Ni^{3+}$) *vs.* RHE respectively (Fig. 3a), which are absent in the pure-PtNWs. These redox peaks are widely recognized as the signature of nickel species[31,32], which further confirm that the nickel species were successfully decorated on PtNWs. The integration of the hydrogen absorption desorption region gives a high ECSA of the 106.2 ± 4.5 m^2/g_{Pt} for SANi-PtNWs, nearly comparable to that of the pure-PtNWs, and considerably larger than those the previously reported Pt-Ni(OH)$_2$ based nano-composites (ECSA~20-60 m^2/g_{Pt})[1,4], highlighting it is critical to precisely tune the number and structure of the decorating species to prevent undesired blockage of surface reactive sites and ensure high ECSA.

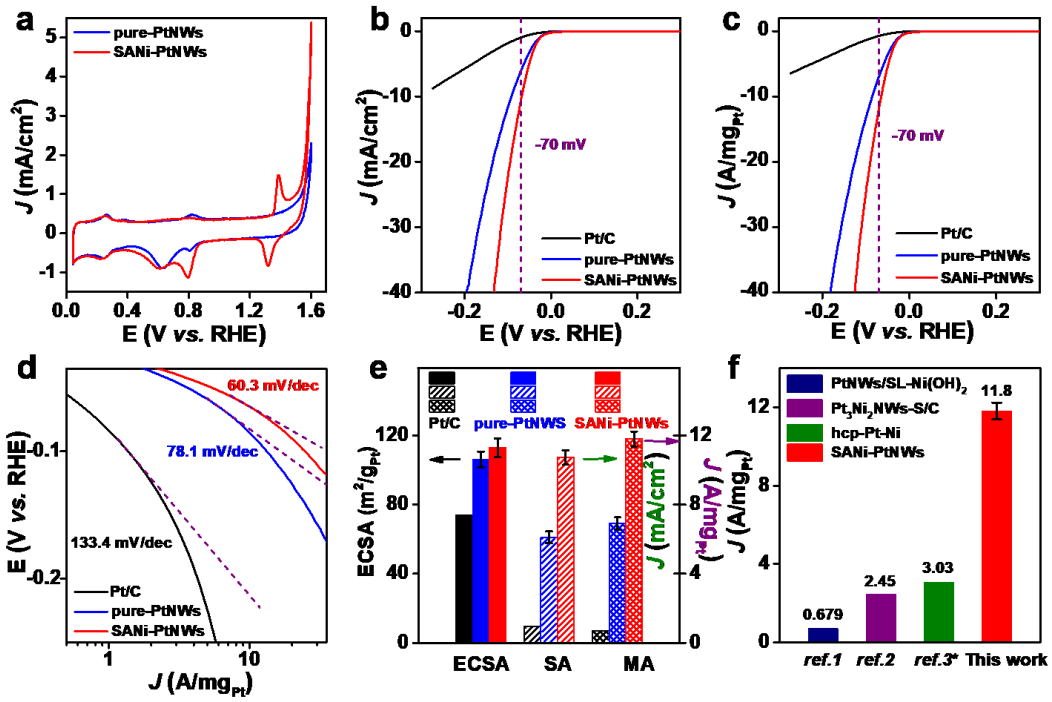

Fig. 3 | Electrocatalytic performance of the SANi-PtNWs for HER compared against Pt/C and pure-PtNWs in 1 M KOH electrolyte. (**a**) Cyclic voltammetry (CV) performed between 0.05 V – 1.60 V *vs.* RHE at a scan rate of 50 mV/s. (**b**) Electrochemically active surface area normalized and (**c**) Pt mass loading normalized HER LSVs with 95% *i*R-compensation at the scan rate of 5 mV/s. (**d**) Pt mass normalized HER Tafel-slope. (**e**) Comparison of ECSA (black arrow to the left), specific activities (normalized by ECSA, green arrow to the right) and mass activities (normalized by Pt mass, purple arrow to the right) for HER at -70 mV vs. RHE for all tested materials. (**f**) Comparison

of HER mass activity of the SANi-PtNWs at -70 mV vs. RHE with the state-of-art values reported previously. * The material in Ref. 3 was tested in 0.1 M KOH. Error bars in e and f indicate the standard deviation of ten independent samples.

The HER performance of SANi-PtNWs was further evaluated using linear sweep voltammetry (LSV) at room temperature in 1 M N_2-saturated KOH with a scan rate of 5 mV/s and compared against commercial Pt/C and pure-PtNWs (Fig. 3b). The specific activities are 0.95, 6.11 ± 0.34, and 10.72 ± 0.41 mA/cm^2 at -70 mV vs. RHE for the Pt/C, pure-PtNWs, and SANi-PtNWs, respectively. It should be noted that the specific activities reported here are normalized to the ECSA, in contrast to the electrode geometrical area used in some previous studies[2]. Meanwhile, the LSV curves normalized by Pt mass give a mass activity of 0.71, 6.90 ± 0.36, and 11.80 ± 0.43 A/mg$_{Pt}$ for Pt/C, pure-PtNWs, and SANi-PtNWs at -70 mV vs. RHE (Fig. 3c). The Tafel diagrams give a Tafel-slope of 60.3 mV/dec for the SANi-PtNWs compared to 78.1 mV/dec for the PtNWs and 133.4 mV/dec for the Pt/C (Fig. 3d), clearly demonstrating the considerably improved HER kinetics with the single Ni atom decorated catalysts.

We have further compared the ECSA, SA and MA of the three different catalysts tested (Fig. 3e). Both the pure-PtNWs and the SANi-PtNWs exhibit a similar ECSA, much higher than that of the Pt/C control. Importantly, the specific activity of the SANi-PtNWs is nearly twice that of the pure-PtNWs, clearly demonstrating that the SANi decoration considerably improves the HER kinetics. Together, with simultaneous achievement of high ECSA and high SA, the SANi-PtNWs deliver a clear leap in mass activity, achieving an MA about 3-10 times higher than those of the state-of-the-art HER catalysts reported to date (Fig. 3F, Table 1). Additionally, at -70 mV *vs.* RHE, SANi-PtNWs showed a specific activity (normalized by ECSA) of 11.8 mA/cm^2 in 4 M KOH (Supplementary Fig. 6a) and 25.7 mA/cm^2 and 48 mA/cm^2 at elevated temperature (313 K and 333 K, Supplementary Fig. 6b), about 9-14 times higher than those of Pt/C. These results indicate the promoted HER activity of SANi-PtNWs is maintained under harsher conditions.

We should also note that the preparation of SANi-PtNWs by interrupted dealloying process is highly repeatable and the resulting materials show consistent performance in 10 independent batches (See supplementary Fig. 2d). Furthermore, chronopotentiometry stability test shows negligible over-potential change for HER when operating at a constant current density of 5 A/mg$_{Pt}$ in 1 M KOH after 4 hours, suggesting such single atomic decoration is stable in the electrochemical processes (Supplementary Fig. 7). The improved HER durability could be partly attributed to multipoint line contacts between the 1D NWs and the carbon support, which prevents physical movement and aggregation (note that the movement and aggregation 0D nanoparticle catalysts contribute significantly to the degrading activities); Additionally, the SANi-PtNWs can effectively reduce the

reaction kinetic barrier, delivering a higher current density at the reduced over-potential, which could also contribute to the durability of the catalyst during long time operation.

Table 1 | Comparing HER performance of SANi-PtNWs and pure-PtNWs *vs.* the state-of-the-art at -70mV *vs.* RHE.

Material	Test condition	ECSA (m^2/g_{Pt})	SA (mA/cm^2)	MA (A/mg_{Pt})
SANi-PtNWs	1 M KOH	**106.2 ± 4.5**	**10.72 ± 0.41**	**11.8 ± 0.43**
pure-PtNWs		112.9 ± 5.4	6.11 ± 0.34	6.90 ± 0.36
PtNWs/SL $Ni(OH)_2$[#]	1 M KOH	27.4	2.48	0.68
Pt_3Ni_2 NWs-S/C[†]	1 M KOH	NA	NA	2.45
hcp-Pt-Ni[§]	0.1 M KOH	26.6	11.41	3.03

[#]Pt nanowires grown on single-layered $Ni(OH)_2$ nanosheets (*1*); [†]PtNi/NiS nanowires (*2*); [§]hcp platinum-nickel alloy excavated nano-multipods (*3*).

Density functional theory calculations of HER activity. To further explore the impact of the SANi species on HER activity, we have conducted density functional theory (DFT) calculations, probing the hydrogen (H) adsorption free energies on a series of model catalytic active sites[33]. We have first considered the fully dealloyed pure-PtNWs that presents a variety of defect sites including atoms with lower and higher metallic coordination than the regular Pt (111) termination. To this end, we constructed representative models of the local surface environments in the form of steps or one-layer concave cavities[21]. Local surface environment at these sites have been described using three models: model ***A*** (Fig. 4a and Supplementary Fig. 8a) and ***B*** (Supplementary Fig. 8b) consisting of different size concave cavities on the Pt (111) surface, and model ***C*** (Supplementary Fig. 8c, d) consisting of a Pt (553) stepped surface.

All the potential adsorption sites for H have been explored on these surfaces, and only the locally stable H structures were considered for evaluating HER activity. To determine which adsorption sites are accessible in the experimental conditions, we explored the occupied adsorption sites as a function of H coverage. The optimal H coverage is determined via first-principle atomistic thermodynamics. The HER activity for all locally stable sites is calculated using a volcano-type kinetic model, which expresses the exchange current i_0 as a function of H adsorption free energy (Fig. 4b)[33]. The activity optimum appears for a site with H-binding energy 0.09 eV weaker than that on the hollow sites occupied on Pt (111)[33]. This model was first proposed for HER in acidic water, but then proven to be also valid for HER in alkaline water[9].

The defective surface models of the dealloyed PtNWs show a large distribution of H binding strengths with a rich population of active sites with binding energy near the optimum value (Fig. 4b). Bridge sites on the ridge of the cavities are clearly more stable

than hollow sites on Pt (111), but accordingly poorly active for HER. The *fcc* sites on the defective surface models are less stable than those on Pt (111) by 0.03 to 0.1 eV and in the uppermost volcano region. Top sites are not stable on Pt (111) (they diffuse to *fcc* hollow sites), but interestingly they become locally stable both inside the cavity and on the upper terrace close to the ridge on the defective models (see T1 and T2 on model ***A*** for example). These top sites show a weaker H-binding energy *vs.* hollow sites on Pt (111) and are placed in the highly active zone.

When considering all sites together, the H atoms will first occupy the inactive bridge sites at low coverage, and then occupy the active top and *fcc* hollow sites with increasing coverage. It is hence crucial to determine the H coverage in realistic conditions. The total adsorption free energy at different H coverage is shown in Fig. 4c as a function of the electrode potential *vs.* RHE (U_{RHE}). For model ***A***, in pH=14 solution, a low coverage (1/16 ML) is favored for a $U_{RHE} > 0.40$ V, while below 0.25 V the H coverage strongly rises to 9/16 ML (occupation of 3 B1 sites and 6 B2 sites in Fig. 4a). For a potential below 0.10 V, sites that are more active than Pt (111) begin to be populated (3 F sites, 3 T2 sites and 1 T1 site). At the experimental potential of -70 mV vs. RHE, a high coverage of 1 ML is reached, with occupation of both active (7/16 ML) and inactive (9/16 ML) sites. The significant density of highly active sites contributes to the high activity of the pure-PtNWs.

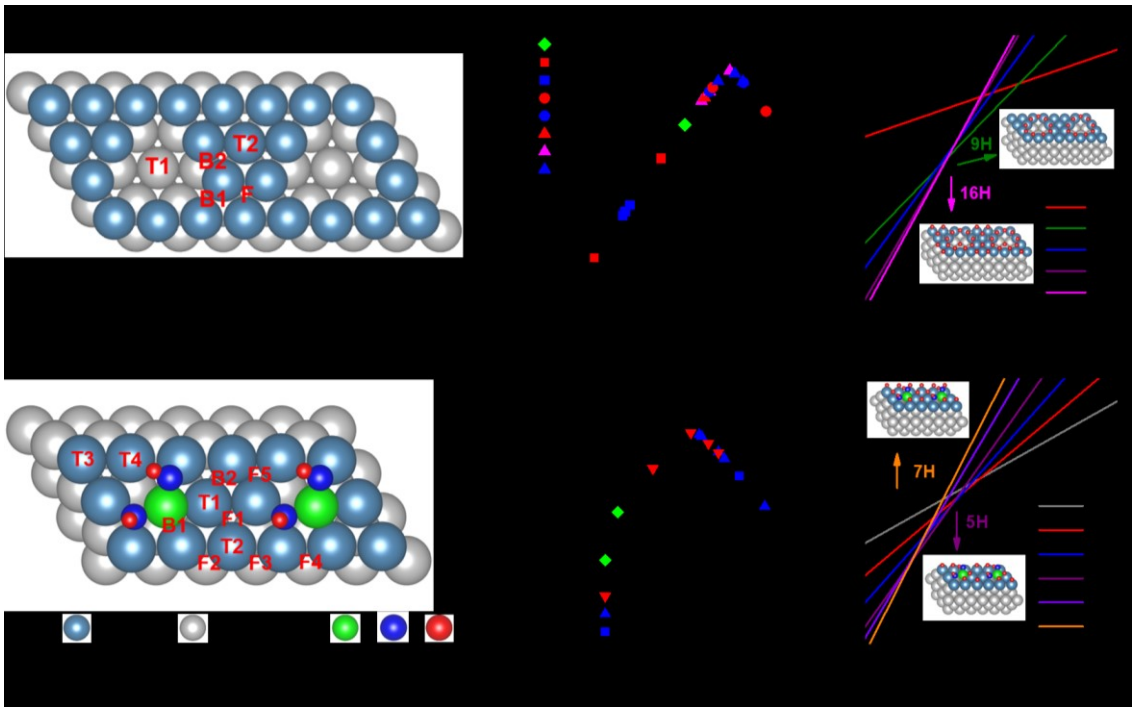

Fig. 4 | Density functional theory (DFT) calculations of the active sites. (**a**) Cavity defect on the Pt (111) surface (Model A). The unit cell is 4×4, and the figure shows 2 unit cells. The locally stable adsorption sites for the H atom are labeled on the top view model. (**b**) Exchange current i_0 for HER as a function of *H adsorption free energy for the locally stable adsorption sites in Models *A*, *B* and *C* (The structures of Model *B* and *C* are shown in Supplementary Fig. 8b-d). (**c**) Adsorption free

energy of hydrogen on model A Pt surface as a function of the applied potential U_{RHE} at various coverage in pH=14 solution. (**d**) Model D for SANi decorated Pt (111) surface, Ni atom being in the surface layer. The unit cell is 3×3, and the figure shows 2 unit cells. (**e**) Volcano curve for adsorption sites on model D at low coverage (LC) and high coverage (HC) conditions. (**f**) Adsorption free energy of hydrogen on model D as a function of U_{RHE} at various coverage at pH=14.

In addition to the models of defective surface, the influence of SANi on the surface is modeled by inserting single Ni atoms in the first layer of a Pt (111) surface. In the considered basic conditions, two OH groups bind with surface Ni atom (Fig. 4d), in line with experimental data (Fig. 2e, Supplementary Table 3). Fig. 4e shows the HER activity predicted from the volcano curve for the stable adsorption sites at low and high H coverage conditions. DFT calculations demonstrate that such SANi species electronically modify the Pt atoms in their surroundings, decreasing their H bind energy to the nearly optimal HER activity region. At low coverage condition (≤ 5/9 ML), H adsorbs preferentially on Pt-Ni bridge site B1 (Fig. 4d) and then on the top Pt sites (T1-T4); while at high coverage (>5/9 ML), occupation of bridge sites B1 and B2 together with slightly less stable hollow sites F1-F5 becomes favored over top site occupations (Supplementary Fig. 8e). Notably, all the sites in the SANi decorated Pt surface as shown in Fig. 4d are more active than those without SANi decoration. At experimental condition (-70 mV *vs.* RHE), the optimal coverage is 5/9 ML (Fig. 4f), which means the B1 bridge site and T1-T4 top sites are occupied by H (black and red marks in Fig. 4e).

One should note that the OH ligands are crucial for the enhanced HER activity: a single bare Ni atom does not produce this favorable electronic modification (Supplementary Fig. 8f). All the additional DFT models and the adsorption free energies for all the models are shown in Supplementary Figs. 8g-i, Supplementary Fig. 9 and Supplementary Table 3 respectively. It is important to note that the SANi species only significantly enhances the nearest neighboring Pt sites. In this regard, the surface decoration by the well-distributed SANi is indeed highly desired for generating most activated Pt sites without unnecessarily blocking too many Pt sites to achieve optimized mass activity. Larger clusters of nickel species would have much fewer neighboring Pt sites and also block more surface Pt sites (Supplementary Fig. 1b).

MOR/EOR activities of the SANi-PtNWs. To further explore the SANi-PtNWs as multifunctional electrocatalysts, we have evaluated their performance for methanol oxidation reactions (MOR) and ethanol oxidation reactions (EOR). The SANi-PtNWs were prepared in the same way as those described in the HER experiments. The MOR test was conducted in aqueous electrolyte with 1 M methanol and 1 M KOH. Cyclic voltammetry (CV) with a scan rate of 20 mV/s were used to evaluate catalytic properties of the SANi-PtNWs and compared with that of the pure-PtNWs and the Pt/C under the same test conditions. Importantly, the Pt mass normalized CV curve shows a peak current

density of 7.93 ± 0.45 A/mg_{Pt} at 0.816 V *vs.* RHE (Fig. 5a), more than 7 and 2 times those of the commercial Pt/C (1.04 A/mg_{Pt}) and the pure-PtNWs (3.87 A/mg_{Pt}), respectively. Additionally, a 144 mV decrease of the onset overpotential (defined as overpotential required to reach a mass activity reach of 0.1 A/mg_{Pt}) is observed in the SANi-PtNWs when compared with that of Pt/C, suggesting the lower activation barrier of methanol oxidation on the SNAi-PtNWs surface (Figure 5a). Similarly, the EOR test in 1 M ethanol/1 M KOH solution shows a peak mass activity of 5.60 ± 0.27 A/mg_{Pt} at 0.785V *vs.* RHE for the SANi-PtNWs (Fig. 5b), which is more than 7 and 3 times higher than those of the Pt/C and the pure-PtNWs, respectively. Additionally, a 61 mV decrease of the onset overpotential is also observed for the SANi-PtNWs vs. Pt/C reference.

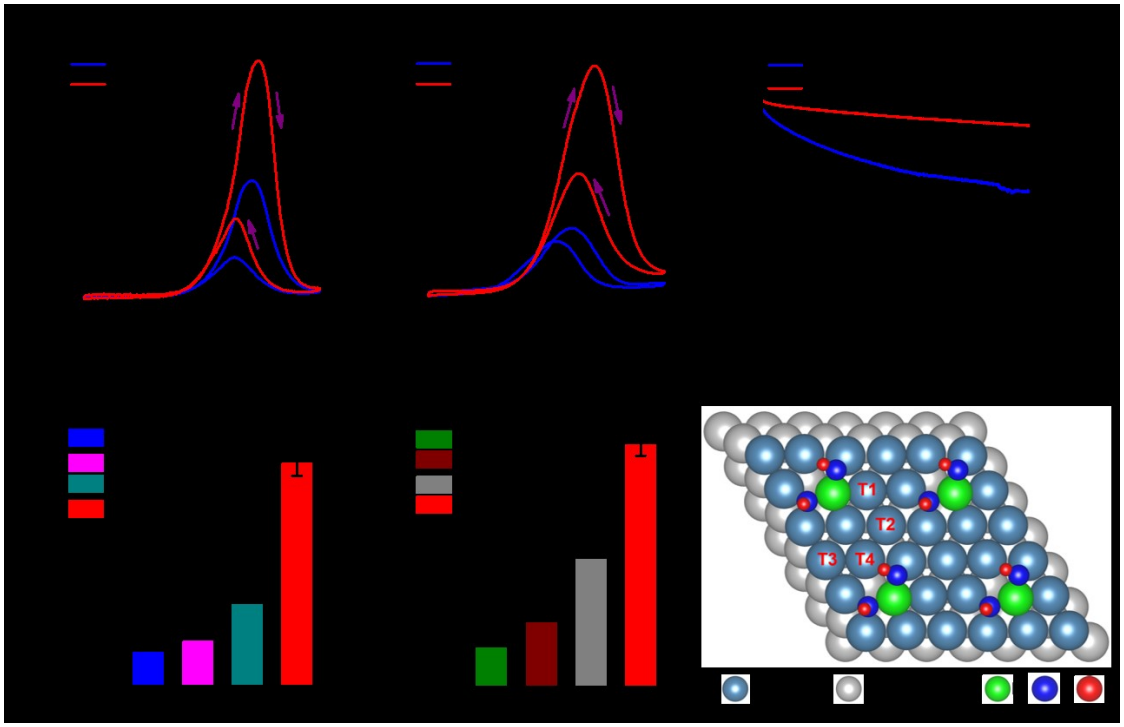

Fig. 5 | MOR and EOR electrocatalytic activities of the SANi-PtNWs, pure-PtNWs, and Pt/C in 1 M KOH electrolyte. (**a**) The MOR CVs under sweeping rate of 20 mV/s, the concentration of methanol is 1 M. (**b**) The EOR CVs under sweeping rate of 20 mV/s, the concentration of ethanol is 1 M. (**c**) The chronoamperometry MOR test at the potential of 0.65 V *vs.* RHE. (**d**) The MOR and (**e**) EOR peak mass activity comparison with the state-of-art values reported recently. Error bars in d and e indicate the standard deviation of ten independent samples. *The material in *ref. 6* was tested in 0.5 M KOH and 2 M methanol, and that in *ref. 8* was tested in 0.5 M NaOH. (**f**) Model D for SANi decorated Pt (111) surface with different CO adsorption sites labeled as T1, T2, T3 and T4.

The chronoamperometry (CA) tests were used to evaluate the stability of SANi-PtNWs, pure-PtNWs and Pt/C in MOR (Fig. 5c). Apparently, the MOR activity of the Pt/C benchmark material shows a rather rapid decay to 0.056 A/mg_{Pt} after 3600 s CA test at 0.650V *vs.* RHE. In contrast, the SANi-PtNWs shows a relatively stable mass activity 0.76 A/mg_{Pt} after 3600 s CP test under the same conditions, clearly demonstrating

the superior stability of SANi-PtNWs catalysts when compared to the Pt/C. The pure-PtNWs also show a faster activity decay to 0.26 A/mg_{Pt} after 3600 s CA test (*vs.* 0.76 A/mg_{Pt} for the SANi-PtNWs). The studies demonstrate that the SANi decoration not only boosts the activity, but also improves the durability.

We have further conducted DFT calculations to probe the origin of activity/stability enhancement by SANi decoration. A major path for catalyst deactivation in MOR is the poisoning by CO intermediates. On the model D consisting of a $Ni(OH)_2$ decorated Pt (111) surface (Fig. 5f), the DFT calculations clearly indicate that all steps in the reaction pathway are exothermic at the experimental potential (Supplementary Fig. 10) and that the CO adsorption on SANi-modified Pt top sites is 0.06 eV – 0.28 eV weaker than that on Pt (111) top site (Supplementary Table 4 and Figure 5f), hence facilitating the final step conversion from CO to CO_2. Furthermore, we have conducted CO stripping experiments to probe the CO binding strength of different catalysts (Supplementary Fig. 11). The CO stripping experiments show that the SANi-PtNWs exhibit a 52 mV and 88 mV decrease of the onset potential, and 8 mV and 38 mV decrease of CO oxidation peak potential compared to the cases of pure-PtNWs and Pt/C respectively. These results are largely consistent with the DFT calculations and suggest that the enhanced activity and durability for MOR/EOR could be at least partly attributed to the change in CO binding strength upon SANi modification, hence effectively mitigating catalyst poisoning issue. This understanding further demonstrates the exciting potential of the single atom tailoring in modifying the kinetics of MOR or EOR.

Comparing with the state-of-art Pt or PtRu-based MOR catalysts tested under the same conductions, the SANi-PtNWs catalysts show the highest specific activity and mass activity reported to date, to the best of our knowledge, with the mass activity achieved in the SANi-PtNWs catalysts ~3-6 times of the state-of-art values reported recently (Fig. 5d). Comparing with all EOR catalysts reported to date, the SANi-PtNWs also show considerable advantage in mass activity (Fig. 5e), about 2-6 times of the best values reported recently. Together, these studies clearly demonstrate that SANi tailored pure-PtNWs presents a major leap for both MOR and EOR, offering significant potential for future alkaline anion exchange membrane fuel cells development.

Discussion

Together, we have designed an effective approach to tailor Pt nanocatalysts with single atomic nickel (SANi) species. By combining XANES, EXAFS analyses with atomic scale STEM and EELS mapping studies, we verify that the PtNW surface was successfully modified with surface SANi. Electrocatalytic test revealed that the resulting SANi modified Pt nanocatalysts exhibit considerably improved HER performance when compared with the state-of-art HER catalysts. Density functional theory calculations

demonstrate that the single Ni atoms, liganded by two hydroxyl groups, electronically promote the neighboring Pt atoms and enhance their activity towards HER. Our studies suggest that an optimum decoration density (surface Ni:Pt ratio ~1:6) is critical for maximizing specific activity while retaining a high ECSA. This decoration density can be readily tuned, in a fully repeatable way, by our gradual dealloying process but is difficult to achieve with other direct synthetic approaches. Additional MOR and EOR electro-catalytic studies further demonstrate greatly improved mass activities for these reactions. It is important to note that the mass activities achieved in SANi-PtNWs not merely surpass previous works, but also represent a conceptual advance over the state-of-art, with the Pt mass activities for HER, MOR and EOR about 4-20, 3-6, and 2-6 times higher than the state-of-art values reported recently.

Our previous studies have shown that the fully dealloyed pure-PtNWs show high activity for ORR[10], which can be largely attributed to their defective surface featuring rich atomic vacancies and strain[34-36]. As we demonstrated with pure-PtNWs both experimentally and theoretically, these surface features can also contribute to improved activity for HER, MOR and EOR when compared with Pt/C reference. Taking a step further, the current study further explores single atom decoration as a general strategy for tailoring the local electronic structure of Pt catalysts to achieve further enhanced specific activity for a series of technological relevant electrochemical reactions at little or no sacrifice of the surface area, and thus delivering optimized mass activity that is critical for practical applications. The significant enhancement of mass activity for various electrocatalytic systems clearly demonstrates that the surface decoration with single atoms offers an effective and general strategy for tailoring precious metal catalysts for diverse reactions. This strategy of single-atom decoration, by interrupted dealloying, can be expected to be applicable to other dopant elements such as Fe, Co or Cu species.

We should also note that the single-atom tailoring of Pt nanocatalysts is also conceptually distinct from typical single-atom catalysts intensively explored recently. In a typical single-atom catalyst, single metallic atoms are often dispersed on a host substrate with the single metal atoms functioning as the primary active sites[37-40]. To the opposite, in our case, single metal atoms decorate the surface of precious metal Pt catalysts to modify the local atomic configuration and electronic structures of surrounding Pt atoms, thus tailoring their catalytic activity for specific reactions. Here single metal atoms are not the primary active sites but play a critical role as a promoter to enhance the activity of the Pt-based catalysts without significantly blocking the surface active sites, thus defining a general strategy for creating multifunctional electro-catalysts with optimized surface area, specific activity, and mass activity at the same time.

Methods

Synthesis of PtNi alloy NWs. All chemicals were purchased from Sigma-Aldrich unless otherwise specified. In a typical synthesis, 20 mg $Pt(acac)_2$ and 40 mg $Ni(acac)_2$ were mixed with 130 mg glucose, 1.7 mg $W(CO)_6$ and 60 mg PVP-40 in a glass vial, with 5 ml of oleylamine and octadecene (3:2 volume ratio) as co-solvent. The mixture was heated to 140 ºC for 6 hours to form Pt-NiO core-shell nanowires. The result nanowires were collected via centrifuge at 7000 rpm for 20 min. After loading the nanowires on carbon black, the catalysts were then annealed under 450 ºC in argon/hydrogen (97:3) atmosphere for 12 hours to obtain the PtNi alloy nanowires supported on carbon black.

Material Characterizations.

High spatial resolution STEM-EELS experiments were conducted by Nion UltraSTEM-200, equipped with C3/C5 corrector and high-energy resolution monochromated EELS system. The instrument was operated at 60 kV with a convergence semi-angle of 30 mrad and a beam current of ~100 pA. HAADF-STEM imaging was performed using an inner and outer collection semi-angle of 70 and 210 mrad. EELS measurement was carried out using a dispersion of 0.26 eV/channel and the dwell time of 0.5 s/pixel. Background in each spectrum was removed by power-law function in commercial software package Digital Micrograph.

X-ray absorption data analysis. The X-ray absorption fine structure spectra for Ni K-edge and Pt L-edge EXAFS data were recorded at the microprobe beamline 10.3.2 of the Advanced Light Source (ALS), Lawrence Berkeley National Laboratory (LBNL). The storage ring was operated in top-off mode (1.9 GeV and 500 mA). Using a Si (111) monochromator, the data collection was carried out in fluorescence mode for all samples under ambient conditions. The beam spot size was 15×3 μm^2 for XANES and EXAFS measurements.

The acquired EXAFS data were processed according to the standard procedures using the ATHENA module implemented in the IFEFFIT software packages. The k^3-weighted EXAFS spectra were obtained by subtracting the post-edge background from the overall absorption and then normalizing with respect to the edge-jump step. Subsequently, k^3-weighted $\chi(k)$ data were Fourier transformed to real (R) space using a hanning windows (dk=1.0 $Å^{-1}$) to separate the EXAFS contributions from different coordination shells. To obtain the quantitative structural parameters around central atoms, least-square curve parameter fitting was performed using the ARTEMIS module of the IFEFFIT software packages.

The following EXAFS equation was used:

$$\chi(k)=\sum_j \frac{N_j S_o^2 F_j(k)}{k R_j^2}\exp[-2k^2\sigma_j^2]\exp[\frac{-2R_j}{\lambda(k)}]\sin[2kR_j+\phi_j(k)] \quad (1)$$

S_0^2 is the amplitude reduction factor, $F_j(k)$ is the effective curved-wave backscattering amplitude, N_j is the number of neighbors in the j^{th} atomic shell, R_j is the distance between the X-ray absorbing central atom and the atoms in the j^{th} atomic shell (backscatterer), λ is the mean free path in Å, $\phi_j(k)$ is the phase shift (including the phase shift for each shell and the total central atom phase shift), σ_j is the Debye-Waller parameter of the j^{th} atomic shell (variation of distances around the average R_j). The functions $F_j(k)$, λ and $\phi_j(k)$ were calculated with the *ab initio* code FEFF8.2.

Electrochemical measurements for HER. To prepare the SANi-PtNW catalyst ink, 2 mg catalysts (SANi-PtNWs on Vulcan 72 carbon black) were dispersed in 2 mL pure ethanol. 20 μL Nafion 117 solution was added to the ink as the binder. 30 μL ink was drop-cast on the glassy carbon electrode (0.196 cm^2). For Pt/C, 2 mg Pt/C (10% Pt/C purchased from Alfa Aesar) were dispersed in 2 mL pure ethanol, with 20 μL Nafion 117 solution added as the binder. 10 uL Pt/C ink was drop-cast on the glassy carbon electrode (0.196 cm^2). The Pt loading on RDE for Pt/C, pure-PtNWs, and SANi-PtNWs was 3.0 μg/cm^2, 2.0 μg/cm^2, and 2.0 μg/cm^2 respectively for RDE test. Alkaline/mercury oxide electrode was used as the reference electrode, and graphite rod was used as the counter electrode. The reference electrode calibration was completed in H_2-saturated 1 M KOH at room temperature. 1600 rpm rotation speed was applied on working RDE to get rid of generated bubble during the performance test. The ECSA was determined by H_{upd} at 0.05 V – 0.35 V vs. RHE in 0.1 M $HClO_4$. The specific and mass current densities were normalized by the ECSA and total Pt loading.

Electrochemical measurements for MOR and EOR. Alkaline/mercury oxide electrode was used as the reference electrode, and graphite rod was used as the counter electrode. The reference electrode calibration was completed in H_2-saturated 1 M KOH at room temperature. 1 M methanol and ethanol were added in to the electrolyte as the reactant for MOR and EOR, respectively. The Pt loading on RDE for Pt/C, pure-PtNWs, and SANi-PtNWs was 3.0 μg/cm^2, 3.47 μg/cm^2, and 3.47 μg/cm^2, respectively. The ECSA was determined by H_{upd} at 0.05 V – 0.35 V vs. RHE in 0.1M $HClO_4$. The specific and mass current densities were normalized by the ECSA and total Pt loading.

Electrochemical measurements for acidic CO stripping. The CV dealloying cycles were interrupted at 10^{th}, 50^{th}, 100^{th}, 150^{th}, 180^{th} and 200^{th} cycles. Before each CO stripping measurement, we firstly performed chronoamperometry at 0.05 V *vs.* RHE in CO saturated electrolyte (0.1 M $HClO_4$) for 10 min. Then we performed chronoamperometry at 0.05 V *vs.* RHE in N_2 saturated electrolyte (0.1 M $HClO_4$) for 10 min. The CO stripping CV scan range was set in 0.05 V to 1.1 V vs. RHE with a positive-scan starting direction. The scan rate was

set to 50 mV/s. Ag/AgCl electrode was used as the reference electrode, and graphite rod was used as the counter electrode.

Electrochemical measurements for alkaline CO stripping. For alkaline CO striping experiment, we first performed chronoamperometry at 0.05 V *vs.* RHE in CO saturated electrolyte (1 M KOH) for 15 min. After the current reached to a steady state, we then performed chronoamperometry at 0.05 V *vs.* RHE in N_2 saturated electrolyte (1 M KOH) for 10 min. The CO stripping CV scan range was set between 0.05 V to 1.1 V *vs.* RHE with a positive-scan starting direction. The scan rate was set to 25 mV/s. alkaline/mercury oxide electrode. The graphite rod was used as the counter electrode.

Computational details

All the DFT calculations are carried out by *VASP*[41,42] with the PBE exchange correlation functional[43]. The one electron wavefunction is developed on a plane wave basis set with a 450 eV energy cut-off. The reciprocal space is sampled using a 5×5×1 K-point grid for systems with 4×4 or 5×5 unit cell, and 7×7×1 K-points for systems with 3×3 unit cell. All model slabs contain 5 layers. For the models with cavities, the top three layers are fully relaxed, while for the models with $Ni(OH)_2$ decoration, the top two layers are relaxed. The convergence threshold on atomic forces is 0.01 eV/Å.

Calculation of adsorption free energy

The adsorption free energy of H_2 is calculated by equation (2):

$$\Delta G_{nH} = G(\text{slab}+n\text{H}) - G(\text{slab}) - \frac{n}{2}G(\text{H}_2) \quad (2)$$

G is the Gibbs free energy, and n is the number of adsorbed H atoms. We used the following equations to calculate the free energies:

$$G(\text{slab}+n\text{H}) = E(\text{slab}+n\text{H}) + ZPE\ (n^*\text{H}) + TS_{\text{vib}}(n^*\text{H}) \quad (3)$$

$$G(\text{slab}) = E(\text{slab}) \quad (4)$$

$$\text{G}(\text{H}_2) = \text{E}(\text{H}_2) + ZPE(\text{H}_2) + TS(\text{H}_2) \quad (5)$$

In equation (3), E(slab+nH) is the electronic energy of the metal slab with adsorbed H atoms, *H means the adsorbed H atom, ZPE (n*H) means the zero point energy of n adsorbed H atoms, T is the temperature, and S_{vib} is the vibrational entropy. The latter two terms are calculated from the vibrational frequencies ν_i of the adsorbed H atoms by using equations (6) and (7):

$$ZPE(n^*\mathrm{H}) = \sum_{i=1}^{3n} \frac{h\nu_i}{2} \quad (6)$$

[redacted] (7)

When calculating the vibrational frequencies of multiple adsorbed H atoms, the slab thickness was reduced by one layer to reduce the computational cost.

Relative free energy with respect to Pt (111) $\Delta G_H - \Delta G_H^{Pt(111)}$ ($\Delta\Delta G$), are calculated using a 5 layer Pt (111) surface with 4×4 unit cell.

Calculation of adsorption free energy in the solution with the effect of applied potential and pH.

$$\Delta G = G(\mathrm{slab}+n\mathrm{H}) - G(\mathrm{slab}) - \frac{n}{2}G(\mathrm{H_2}) - n\mu_{H^++e^-} \quad (8)$$

$$\mu_{H^++e^-} = -eU_{SHE} - 2.3kTpH \quad (9)$$

We used equation (8) to calculate the adsorption free energy with the impact of the reduction potential on the electrode, where the first three terms on the right side are the same as the terms in equation (2), the term $\mu_{H^++e^-}$ is the chemical potential of hydrogen ion and electron, which is calculated using equation (9)[44]. U_{SHE} is the potential vs. standard hydrogen electrode.

Structures

The atomic coordinates of the optimized computational models are all provided as a text file in supplementary information.

Data availability. The data that support the findings of this study are available from the corresponding authors on reasonable request.

References

1 Yin, H., Zhao, S., Zhao, K., Muqsit, A., Tang, H., Chang, L., Zhao, H., Gao, Y. & Tang, Z. Ultrathin platinum nanowires grown on single-layered nickel hydroxide with high hydrogen evolution activity. *Nat. Commun.* **6**, 6430 (2015).

2 Wang, P., Zhang, X., Zhang, J., Wan, S., Guo, S., Lu, G., Yao, J. & Huang, X. Precise tuning in platinum-nickel/nickel sulfide interface nanowires for synergistic hydrogen evolution catalysis. *Nat. Commun.* **8**, 14580 (2017).

3 Cao, Z., Chen, Q., Zhang, J., Li, H., Jiang, Y., Shen, S., Fu, G., Lu, B.-a., Xie, Z. & Zheng, L. Platinum-nickel alloy excavated nano-multipods with hexagonal close-packed structure and superior activity towards hydrogen evolution reaction. *Nat. Commun.* **8**, 15131 (2017).

4 Huang, W., Wang, H., Zhou, J., Wang, J., Duchesne, P. N., Muir, D., Zhang, P., Han, N., Zhao, F. & Zeng, M. Highly active and durable methanol oxidation electrocatalyst based on the synergy of platinum–nickel hydroxide–graphene. *Nat. Commun.* **6**, 10035 (2015).

5 Ren, F., Wang, C., Zhai, C., Jiang, F., Yue, R., Du, Y., Yang, P. & Xu, J. One-pot synthesis of a RGO-supported ultrafine ternary PtAuRu catalyst with high electrocatalytic activity towards methanol oxidation in alkaline medium. *J. Mater. Chem. A* **1**, 7255-7261 (2013).

6 Feng, Y.-Y., Bi, L.-X., Liu, Z.-H., Kong, D.-S. & Yu, Z.-Y. Significantly enhanced electrocatalytic activity for methanol electro-oxidation on Ag oxide-promoted PtAg/C catalysts in alkaline electrolyte. *J. Catal.* **290**, 18-25 (2012).

7 Wu, H., Li, H., Zhai, Y., Xu, X. & Jin, Y. Facile Synthesis of Free‐Standing Pd‐Based Nanomembranes with Enhanced Catalytic Performance for Methanol/Ethanol Oxidation. *Adv. Mater.* **24**, 1594-1597 (2012).

8 Ren, F., Wang, H., Zhai, C., Zhu, M., Yue, R., Du, Y., Yang, P., Xu, J. & Lu, W. Clean method for the synthesis of reduced graphene oxide-supported PtPd alloys with high electrocatalytic activity for ethanol oxidation in alkaline medium. *ACS Appl. Mater. Interfaces* **6**, 3607-3614 (2014).

9 Danilovic, N., Subbaraman, R., Strmcnik, D., Chang, K. C., Paulikas, A., Stamenkovic, V. & Markovic, N. M. Enhancing the alkaline hydrogen evolution reaction activity through the bifunctionality of Ni (OH) 2/metal catalysts. *Angew. Chem.* **124**, 12663-12666 (2012).

10 Li, M., Zhao, Z., Cheng, T., Fortunelli, A., Chen, C.-Y., Yu, R., Zhang, Q., Gu, L., Merinov, B. V. & Lin, Z. Ultrafine jagged platinum nanowires enable ultrahigh mass activity for the oxygen reduction reaction. *Science* **354**, 1414-1419 (2016).

11 Chen, C., Kang, Y., Huo, Z., Zhu, Z., Huang, W., Xin, H. L., Snyder, J. D., Li, D., Herron, J. A. & Mavrikakis, M. Highly crystalline multimetallic nanoframes with three-dimensional electrocatalytic surfaces. *Science* **343**, 1339-1343 (2014).

12 Choi, S.-I., Xie, S., Shao, M., Odell, J. H., Lu, N., Peng, H.-C., Protsailo, L., Guerrero,

S., Park, J. & Xia, X. Synthesis and characterization of 9 nm Pt–Ni octahedra with a record high activity of 3.3 A/mgPt for the oxygen reduction reaction. *Nano Lett.* **13**, 3420-3425 (2013).

13 Zhang, Z., Liu, G., Cui, X., Chen, B., Zhu, Y., Gong, Y., Saleem, F., Xi, S., Du, Y. & Borgna, A. Crystal Phase and Architecture Engineering of Lotus‐Thalamus‐Shaped Pt‐Ni Anisotropic Superstructures for Highly Efficient Electrochemical Hydrogen Evolution. *Adv. Mater.*, **30**, 1801741 (2018).

14 Zhang, Z., Luo, Z., Chen, B., Wei, C., Zhao, J., Chen, J., Zhang, X., Lai, Z., Fan, Z. & Tan, C. One‐Pot Synthesis of Highly Anisotropic Five‐Fold‐Twinned PtCu Nanoframes Used as a Bifunctional Electrocatalyst for Oxygen Reduction and Methanol Oxidation. *Adv. Mater.* **28**, 8712-8717 (2016).

15 Zhang, L., Roling, L. T., Wang, X., Vara, M., Chi, M., Liu, J., Choi, S.-I., Park, J., Herron, J. A. & Xie, Z. Platinum-based nanocages with subnanometer-thick walls and well-defined, controllable facets. *Science* **349**, 412-416 (2015).

16 van der Vliet, D. F., Wang, C., Li, D., Paulikas, A. P., Greeley, J., Rankin, R. B., Strmcnik, D., Tripkovic, D., Markovic, N. M. & Stamenkovic, V. R. Unique Electrochemical Adsorption Properties of Pt‐Skin Surfaces. *Angew. Chem.* **124**, 3193-3196 (2012).

17 Cui, C., Gan, L., Heggen, M., Rudi, S. & Strasser, P. Compositional segregation in shaped Pt alloy nanoparticles and their structural behaviour during electrocatalysis. *Nat. Mater.* **12**, 765-771 (2013).

18 Zhang, J., Lima, F., Shao, M., Sasaki, K., Wang, J., Hanson, J. & Adzic, R. Platinum monolayer on nonnoble metal− noble metal core− shell nanoparticle electrocatalysts for O2 reduction. *J. Phys. Chem. B* **109**, 22701-22704 (2005).

19 Fu, X.-Z., Liang, Y., Chen, S.-P., Lin, J.-D. & Liao, D.-W. Pt-rich shell coated Ni nanoparticles as catalysts for methanol electro-oxidation in alkaline media. *Catal. Commun.* **10**, 1893-1897 (2009).

20 Calle-Vallejo, F., Tymoczko, J., Colic, V., Vu, Q. H., Pohl, M. D., Morgenstern, K., Loffreda, D., Sautet, P., Schuhmann, W. & Bandarenka, A. S. Finding optimal surface sites on heterogeneous catalysts by counting nearest neighbors. *Science* **350**, 185-189 (2015).

21 Calle-Vallejo, F., Pohl, M. D., Reinisch, D., Loffreda, D., Sautet, P. & Bandarenka, A. S. Why conclusions from platinum model surfaces do not necessarily lead to enhanced nanoparticle catalysts for the oxygen reduction reaction. *Chem. Sci.* **8**, 2283-2289 (2017).

22 Huang, X., Zhao, Z., Cao, L., Chen, Y., Zhu, E., Lin, Z., Li, M., Yan, A., Zettl, A. & Wang, Y. M. High-performance transition metal–doped Pt3Ni octahedra for oxygen reduction reaction. *Science* **348**, 1230-1234 (2015).

23 Strasser, P., Koh, S., Anniyev, T., Greeley, J., More, K., Yu, C., Liu, Z., Kaya, S., Nordlund, D. & Ogasawara, H. Lattice-strain control of the activity in dealloyed core–shell fuel cell catalysts. *Nat. Chem.* **2**, 454-460 (2010).

24 Cui, C., Gan, L., Li, H.-H., Yu, S.-H., Heggen, M. & Strasser, P. Octahedral PtNi

nanoparticle catalysts: exceptional oxygen reduction activity by tuning the alloy particle surface composition. *Nano Lett.* **12**, 5885-5889 (2012).

25 Subbaraman, R., Tripkovic, D., Chang, K.-C., Strmcnik, D., Paulikas, A. P., Hirunsit, P., Chan, M., Greeley, J., Stamenkovic, V. & Markovic, N. M. Trends in activity for the water electrolyser reactions on 3d M (Ni, Co, Fe, Mn) hydr (oxy) oxide catalysts. *Nat. Mater.* **11**, 550-557 (2012).

26 Jiang, Q., Jiang, L., Wang, S., Qi, J. & Sun, G. A highly active PtNi/C electrocatalyst for methanol electro-oxidation in alkaline media. *Catal. Commun.* **12**, 67-70 (2010).

27 Subbaraman, R., Tripkovic, D., Strmcnik, D., Chang, K.-C., Uchimura, M., Paulikas, A. P., Stamenkovic, V. & Markovic, N. M. Enhancing hydrogen evolution activity in water splitting by tailoring Li+-Ni (OH) 2-Pt interfaces. *Science* **334**, 1256-1260 (2011).

28 Lytle, F. W. Determination of d-band occupancy in pure metals and supported catalysts by measurement of the LIII X-ray absorption threshold. *J. Catal.* **43**, 376-379 (1976).

29 Pearson, D., Ahn, C. & Fultz, B. White lines and d-electron occupancies for the 3d and 4d transition metals. *Phys. Rev. B* **47**, 8471-8478 (1993).

30 Becknell, N., Kang, Y., Chen, C., Resasco, J., Kornienko, N., Guo, J., Markovic, N. M., Somorjai, G. A., Stamenkovic, V. R. & Yang, P. Atomic structure of Pt3Ni nanoframe electrocatalysts by in situ X-ray absorption spectroscopy. *J. Am. Chem. Soc.* **137**, 15817-15824 (2015).

31 Burke, M. S., Enman, L. J., Batchellor, A. S., Zou, S. & Boettcher, S. W. Oxygen evolution reaction electrocatalysis on transition metal oxides and (oxy) hydroxides: activity trends and design principles. *Chem. Mater.* **27**, 7549-7558 (2015).

32 Bates, M. K., Jia, Q., Doan, H., Liang, W. & Mukerjee, S. Charge-transfer effects in Ni–Fe and Ni–Fe–Co mixed-metal oxides for the alkaline oxygen evolution reaction. *ACS Catal.* **6**, 155-161 (2015).

33 Nørskov, J. K., Bligaard, T., Logadottir, A., Kitchin, J., Chen, J. G., Pandelov, S. & Stimming, U. Trends in the exchange current for hydrogen evolution. *J. Electrochem. Soc.* **152**, J23-J26 (2005).

34 Le Bacq, O., Pasturel, A., Chattot, R., Previdello, B., Nelayah, J., Asset, T., Dubau, L. & Maillard, F. Effect of Atomic Vacancies on the Structure and the Electrocatalytic Activity of Pt ‐ rich/C Nanoparticles: A Combined Experimental and Density Functional Theory Study. *ChemCatChem* **9**, 2324-2338 (2017).

35 Chattot, R. l., Asset, T., Bordet, P., Drnec, J., Dubau, L. & Maillard, F. d. r. Beyond Strain and Ligand Effects: Microstrain-Induced Enhancement of the Oxygen Reduction Reaction Kinetics on Various PtNi/C Nanostructures. *ACS Catal.* **7**, 398-408 (2016).

36 Chattot, R., Le Bacq, O., Beermann, V., Kühl, S., Herranz, J., Henning, S., Kühn, L., Asset, T., Guétaz, L. & Renou, G. Surface distortion as a unifying concept and descriptor in oxygen reduction reaction electrocatalysis. *Nat. Mater.* **17**, 827-834 (2018).

37 Fei, H., Dong, J., Feng, Y., Allen, C. S., Wan, C., Volosskiy, B., Li, M., Zhao, Z., Wang, Y. & Sun, H. General synthesis and definitive structural identification of MN 4 C 4 single-atom catalysts with tunable electrocatalytic activities. *Nat. catal.* **1**, 63-72 (2018).

38 Marcinkowski, M. D., Darby, M. T., Liu, J., Wimble, J. M., Lucci, F. R., Lee, S., Michaelides, A., Flytzani-Stephanopoulos, M., Stamatakis, M. & Sykes, E. C. H. Pt/Cu single-atom alloys as coke-resistant catalysts for efficient C–H activation. *Nat. Chem.* **10**, 325-332 (2018).

39 Back, S., Lim, J., Kim, N.-Y., Kim, Y.-H. & Jung, Y. Single-atom catalysts for CO 2 electroreduction with significant activity and selectivity improvements. *Chem. Sci.* **8**, 1090-1096 (2017).

40 Zhang, H., Liu, G., Shi, L. & Ye, J. Single‐Atom Catalysts: Emerging Multifunctional Materials in Heterogeneous Catalysis. *Adv. Energy Mater.* **8**, 1701343(2018).

41 Kresse, G. & Hafner, J. Ab initio molecular dynamics for liquid metals. *Physical Review B* **47**, 558-561 (1993).

42 Kresse, G. & Hafner, J. Ab initio molecular-dynamics simulation of the liquid-metal–amorphous-semiconductor transition in germanium. *Physical Review B* **49**, 14251-14269 (1994).

43 Perdew, J. P., Burke, K. & Ernzerhof, M. Generalized gradient approximation made simple. *Physical review letters* **77**, 3865-3868 (1996).

44 Hansen, M. H., Jin, C., Thygesen, K. S. & Rossmeisl, J. Finite Bias Calculations to Model Interface Dipoles in Electrochemical Cells at the Atomic Scale. *The Journal of Physical Chemistry C* **120**, 13485-13491 (2016).

Acknowledgements. Y.H. acknowledges support from Office of Naval Research by the grant number of N000141812155. X.D. acknowledges the financial for from National Science Foundation through grant 1800580. T.C. was supported by Collaborative Innovation Center of Suzhou Nano Science & Technology, the Priority Academic Program Development of Jiangsu Higher Education Institutions (PAPD), the 111 Project. W.A.G. was supported by Joint Center for Artificial Photosynthesis, a DOE Energy Innovation Hub, supported through the Office of Science of the U.S. Department of Energy under Award Number DE‐SC0004993. This work used the Extreme Science and Engineering Discovery Environment (XSEDE) which is supported by National Science Foundation grant number ACI‐1053575. J.L. acknowledges National Key R&D Program of China (2017YFA0700104), and National Natural Science Foundation of China (51761165012). STEM experiments were conducted using the facilities in the Irvine Materials Research Institute (IMRI) at the University of California-Irvine. We thank Sirine Fakra for the technical support of EXAFS experiment. This research used resources of the Advanced Light Source, which is a DOE Office of Science User Facility under contract no. DEAC02-05CH11231. R.Y. acknowledges National Natural Science Foundation of China (51525102, 51390475). In this work we used the resources of the National Center for

Electron Microscopy in Beijing. The calculations were performed on Hoffman2 cluster at UCLA Institute for Digital Research and Education (IDRE) and the Extreme Science and Engineering Discovery Environment (XSEDE) which is supported by National Science Foundation grant number ACI - 1053575.

Author Information. Reprints and permissions information is available at www.nature.com/reprints. The authors declare no competing financial interests. Readers are welcome to comment on the online version of the paper. Publisher's note: Springer Nature remains neutral with regard to jurisdictional claims in published maps and institutional affiliations. Correspondence and requests for materials should be addressed to X.D. (xduan@chem.ucla.edu), Y.H. (yhuang@seas.ucla.edu) and P.S. (sautet@ucla.edu).

Author contributions

X.D., Y.H., and P.S. supervised the project and designed the research. X.D., Y.H. and M.L. conceived the idea. M.L. and C.W. performed the synthesis, electrochemical tests and characterizations. K.D. and P.S. conceived and performed the DFT calculations. C.T. and W.G. performed the model simulations. L.Z. and W.C. performed XAS measurements and analysis. J.G. and W.C. provided expertise for XAS analysis. S.D. and X.P. performed the EELS and HAADF-STEM measurements, Z.Z., Y.Z., R.Y., J.L., K.Z., Z.L. assisted with material characterizations. Z.Z., P.L., H.F., M.D., J.H. and H.S., assisted with catalytic measurements. M.L., K.D., C.W., P.S., Y.H. and X.D. co-write the paper. All authors discussed the results and commented on the manuscript.

Competing interests

The authors declare no competing interests.